

# Open Boundary Condition for Particle Simulation in Magnetic Reconnection Research

Hiroaki OHTANI<sup>1,2)</sup> and Ritoku HORIUCHI<sup>1,2)</sup>

<sup>1)</sup>*Department of Simulation Science, National Institute for Fusion Science, Toki 509-5292, Japan*

<sup>2)</sup>*Graduate University of Advanced Studies (SOKENDAI), Toki 509-5292, Japan*

(Received 22 December 2008 / Accepted 1 April 2009)

We develop a three-dimensional electromagnetic Particle Simulation code for investigating driven Magnetic reconnection in an Open system from the kinetic view-point (PASMO). In this paper, we advance a new model for the upstream and downstream boundaries. We succeed in achieving the frozen-in condition for both electrons and ions with high accuracy at the upstream boundary, while we can decrease unphysical noise at the downstream boundary. We compare the simulation results of long and short-simulation boxes to check whether the downstream boundary model fulfills its function. The results of the short-simulation box effectively mimic those of the long-simulation box. Using the new boundary model, we succeed in increasing the accuracy of simulation.

© 2009 The Japan Society of Plasma Science and Nuclear Fusion Research

Keywords: electromagnetic PIC simulation code, open boundary condition, magnetic reconnection

DOI: 10.1585/pfr.4.024

## 1. Introduction

Collisionless magnetic reconnection is widely considered to play an important role in energetically active phenomena in high-temperature plasmas, such as solar flares, planetary magnetospheres, fusion devices, and astrophysical plasmas. Magnetic energy is rapidly converted to kinetic energy, and global magnetic configurations change because of magnetic reconnection. In spite of much research from observations [1,2], experiments [3,4], and theory and simulations [5,6], many basic aspects of the detailed mechanisms of reconnection remain poorly understood.

Magnetic reconnection is generally categorized as driven and spontaneous (undriven) reconnections. In driven reconnection, plasma inflow and magnetic flux are supplied from upstream boundaries and drive reconnection, while in spontaneous reconnection, internal instabilities such as collisionless tearing instability [7–13] trigger reconnection without energy inflow from the boundaries.

A magnetohydrodynamics (MHD) simulation [14–17] is adopted to study the global phenomenon of reconnection under an assumption of electric resistivity. This approach can deal with reconnection phenomenologically, but cannot explain the origin of the electric resistivity. On the other hand, fully kinetic electromagnetic particle-in-cell (PIC) simulation is a powerful tool for investigating reconnection, because it can use a first-principle approach to describe the dynamics in the vicinity of the X-point. The first-principle approach means that both electrons and ions are treated as particles under the basic equations without any assumptions, except the initial and boundary condi-

tions. In the reconnection process, the ideal MHD condition breaks down in the reconnection region, where the magnetic field is dominantly dissipated. To estimate the structure and stability of the reconnection region, fully PIC simulation is indispensable.

Several full PIC simulations employed a periodic boundary condition along the direction of reversed magnetic field [18–23]. If a periodic boundary condition is adopted, it is impossible to ascertain whether reconnection can achieve a steady state, because unphysical collisions between oppositely propagating reconnection jets occur through the periodic boundary. To obtain physically meaningful results by means of a full PIC simulation under a periodic boundary condition, the simulation domain must be sufficiently large, because it must run long enough for the artificial recirculation to approach the reconnection region during the time interval of interest. Thus, this model is not appropriate for studying evolution of the reconnection system over a long timescale.

Although a very large periodic system was used, Fujimoto *et al* proposed a two-and-a-half dimensional electromagnetic particle code using an adaptive mesh refinement (AMR) technique to investigate large-scale behavior of magnetic reconnection [23,24]. The AMR technique subdivides and removes cells dynamically in accordance with a refinement criterion, and it can achieve high-resolution simulations of phenomena that locally include micro-scale processes. The AMR technique as well as the open boundary condition is useful for long-timescale reconnection simulations.

To prevent unphysical recirculation, it is crucial to develop an appropriate open boundary model as the down-

author's e-mail: ohtani@dss.nifs.ac.jp

stream boundary for full PIC simulations. Our group has already investigated reconnection processes, turning our attention to the importance of the open boundary condition using the PArticle Simulation code for Magnetic reconnection in an Open system (PASMO) code [25–33]. It was shown for the first time that a steady-state reconnection was realized in the long-time scale evolution of driven reconnection in a two-dimensional (2-D) open system [25–27]. Several other types of open boundary models have been proposed thus far for investigating driven or spontaneous reconnection as well [34–38]. In our previous studies [28,31,32,39], we improved the 2-D full PIC simulation code in an open system to a three-dimensional (3-D) code. However, the frozen-in condition is slightly broken at the upstream boundary, and unphysical disturbance is faintly generated at the downstream boundary.

In this paper, we propose an advanced model for the driven and open boundary conditions to improve the precision of the simulation. In Sec. 2, we describe the basic equations. In Sec. 3, we briefly discuss the initial conditions. A detailed description and discussion of the advanced open boundary model are reported in Secs. 4, 5, and 6. In this discussion, we compare the results obtained from the new and old models and check whether the new downstream model can effectively mimic a much larger system. Finally, we present the summary and conclusions in Sec. 7.

## 2. Basic Equations

We use a 3-D explicit electromagnetic particle simulation code for the investigation of driven magnetic reconnection [40]. The basic equations to be solved are the equations of motion,

$$\frac{d(\gamma_k \mathbf{v}_k)}{dt} = \frac{q_k}{m_k} \left( \mathbf{E} + \frac{\mathbf{v}_k}{c} \times \mathbf{B} \right), \quad (1)$$

$$\frac{d\mathbf{x}_k}{dt} = \mathbf{v}_k, \quad (2)$$

and the Maxwell equations,

$$\frac{1}{c} \frac{\partial \mathbf{B}}{\partial t} = -\nabla \times \mathbf{E}, \quad (3)$$

$$\frac{1}{c} \frac{\partial \mathbf{E}}{\partial t} = \nabla \times \mathbf{B} - 4\pi \mathbf{j}, \quad (4)$$

$$\nabla \cdot \mathbf{B} = 0, \quad (5)$$

$$\nabla \cdot \mathbf{E} = 4\pi \rho, \quad (6)$$

where  $c$  is the velocity of light, and  $\mathbf{x}_k(t)$ ,  $\mathbf{v}_k(t)$ ,  $m_k$ , and  $q_k$  are the position, velocity, rest mass, and charge of the  $k$ th particle. The relativistic  $\gamma$ -factor of the  $k$ th particle is defined by

$$\gamma_k = 1 / \sqrt{1 - (\mathbf{v}_k \cdot \mathbf{v}_k) / c^2}. \quad (7)$$

Current density  $\mathbf{j}(\mathbf{x}, t)$  and charge density  $\rho(\mathbf{x}, t)$  are calculated by taking a sum of values of all the particles, that is,

$$\mathbf{j}(\mathbf{x}, t) = \sum_{k=1}^N \frac{q_k \mathbf{v}_k(t)}{c} S[\mathbf{x} - \mathbf{x}_k(t)], \quad (8)$$

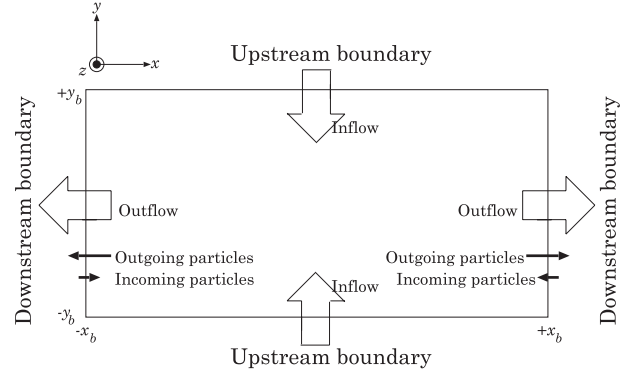


Fig. 1 Schematic illustration of simulation box.

$$\rho(\mathbf{x}, t) = \sum_{k=1}^N q_k S[\mathbf{x} - \mathbf{x}_k(t)], \quad (9)$$

where  $N$  is the total number of particles and  $S(\mathbf{x})$  is the form function of particles. The form function is expressed by a triangle with the base length equal to two times the grid separation.

Only the first two Maxwell equations (Eqs. (3) and (4)) are completely independent. The other two (Eqs. (5) and (6)) always hold if they are initially satisfied. However,  $\mathbf{j}$  and  $\rho$  given by Eqs. (8) and (9) do not exactly satisfy the continuity equation in numerical simulation because of the applicability limits of numerical techniques, such as a finite-sized mesh and weighting [40]. Thus, in our simulation model, we solve the first two Maxwell equations (Eqs. (3) and (4)) for  $\mathbf{E}$  and  $\mathbf{B}$ , and then  $\mathbf{E}$  is adjusted using the correction of the electrostatic part obtained by Boris-type correction [40] to satisfy Eq. (6).

The physical quantities are normalized as follows:  $m = \tilde{m} m_e$ ,  $q = \tilde{q} e$ ,  $t = \tilde{t} / \omega_{ce}$ ,  $v = \tilde{v} c$ ,  $x = \tilde{x} c / \omega_{ce}$ ,  $E = \tilde{E} m_e c \omega_{ce} / e$ , and  $B = \tilde{B} m_e c \omega_{ce} / e$ , where  $m_e$  is the electron mass,  $e$  is the electron charge, and  $\omega_{ce}$  is the electron gyration frequency. We consider a rectangular parallelepiped in  $(x, y, z)$  space as a simulation box, whose length is  $2x_b$ , width is  $2y_b$ , and height is  $2z_b$  (Fig. 1).

## 3. Initial Conditions

The initial condition of the magnetic field,  $B_x$ , pressure  $P$ , current density  $j_z$  and particle density  $n_p$  is given by a one-dimensional Harris-type equilibrium [41] as

$$B_x(y) = B_0 \tanh(y/L), \quad (10)$$

$$P(y) = (B_0^2 / 8\pi) \text{sech}^2(y/L), \quad (11)$$

$$j_z(y) = -(c B_0 / 4\pi L) \text{sech}^2(y/L), \quad (12)$$

$$n_p(y) = n_{p0} / \cosh^2(y/L), \quad (13)$$

where a neutral sheet is located at  $y = 0$ ,  $B_0$  and  $n_{p0}$  are constants, and  $L$  is the spatial scale. The velocity distribution of particles is a shifted Maxwellian, and the uniform average velocity of an ion is equal to the diamagnetic drift

velocity. In this paper, the ion-electron temperature ratio is taken as  $T_{i0}/T_{e0} = 1$  at the initial time.

The particle density described by Eq. (13) becomes very small in the region far from the current sheet, and the number of particles per cell in this region is extremely small compared with that in the current sheet. If the number is small ( $< 10$ ), numerical noise is generated. To reduce numerical noise near the boundary layer, we assume background plasmas with no average velocity and uniform temperature. Two types of distribution of background plasmas are considered, uniform and non-uniform [42]. In the case of uniform distribution, ion-ion kink instability can be caused by the velocity difference between the foreground and background plasmas in the current sheet [43]. To avoid the growth of such instability, we adopt a non-uniform background,

$$n_b(y) = n_{b0}\{1 - 1/\cosh^2(y/L)\}, \quad (14)$$

where  $n_{b0}$  is a constant. Although a weak pressure imbalance appears in this non-uniform background profile, it is quickly justified without any significant modification of the current sheet structure. In this paper, the value of ratio  $n_{b0}/n_{p0}$  is 0.2 at the initial time.

## 4. Boundary Conditions

Let us consider collisionless reconnection in an open system that is subject to an external driving source. It is necessary to develop two boundary models for such a system, i.e., an upstream boundary ( $y$ ) and downstream boundary ( $x$ ). At the upstream boundary, plasma and magnetic flux are supplied into the system, while plasma can move in and out freely at the downstream boundary according to the dynamical evolution of the system. A periodic boundary condition is applied in the  $z$ -direction for both fields and particles.

### 4.1 Boundary conditions of fields

The conditions of the field quantities for the driven and open boundary conditions are given as follows. The external field  $E_{zd}(x, t)$  is programmed to evolve from zero to a constant value during an early period, as shown in Fig. 2. The field  $E_{zd}$  is set as zero at  $t = 0$  and gradually increases, predominantly in the center region of the simulation box ( $x = 0$ ) early in the simulation. The width of the region where  $E_{zd}$  predominantly increases is also gradually expanded. The field  $E_{zd}$  develops on the entire boundary after it reaches a constant value  $E_0$  at the center point, and eventually reaches  $E_0$  on the entire boundary. After an early phase ( $t\omega_{ce} = 335$  in this paper),  $E_{zd}$  has a constant value  $E_0$ , which is a necessary condition for a reconnection system to evolve toward a steady state [26, 27]. Boundary conditions for the remaining field quantities at upstream boundary are as follows:  $E_x = 0$  and  $\partial_y E_y = 0$  at  $y = \pm y_b$ . At the downstream boundary  $x = \pm x_b$ , the field quantities,  $\partial_x E_x$ ,  $\partial_x B_y$  and  $\partial_x B_z$  are zero. These condi-

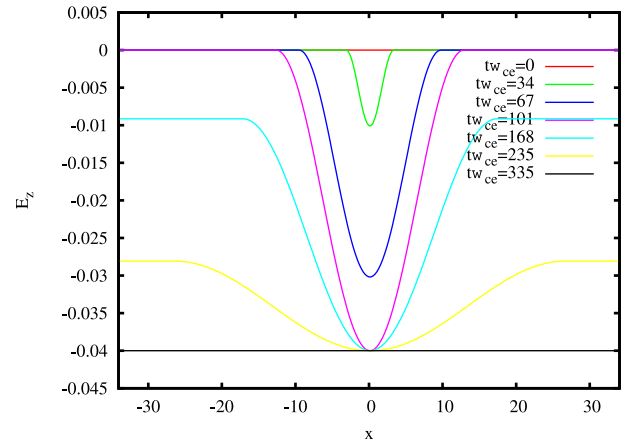


Fig. 2 The spatial profiles of the external driving electric field at the upstream boundary at the times  $t\omega_{ce} = 0, 34, 67, 101, 168, 235$  and  $335$ .

tions enable the  $y$  and  $z$  components of the magnetic field to change, which is a necessary condition for a magnetic island with instability along the  $z$ -direction to move freely through the boundary. The remaining components of the field quantities are obtained by solving the Maxwell equations at the boundary.

### 4.2 Boundary conditions of particles

The free boundary condition of particles is important in constructing the open boundary model [25, 26, 39]. Although noise problems near the system boundary are inevitable in PIC simulations, we propose an advanced model to reduce the noise. Using a new model of the upstream boundary, the frozen-in condition is satisfied at the boundary for both ions and electrons with high accuracy. At the downstream boundary, the particle distribution becomes smooth, and the deviation from the frozen-in condition due to unphysical noise is suppressed at a lower level. We describe the previous and improved new models of the boundaries in this section, and compare the simulation results obtained from the two models in Sec. 5.

#### 4.2.1 Upstream boundary

We suppose that the upstream boundary is an ideal MHD region, where both ions and electrons are frozen into the magnetic field. Thus, the plasma inflow is driven by  $\mathbf{E} \times \mathbf{B}$  drift due to the driving electric field  $E_{zd}(x, t)$  imposed at the upstream boundary. The distribution of input particles is a shifted Maxwellian with a constant temperature and an average velocity  $\mathbf{u}_u$  that is given as

$$\mathbf{u}_u = \frac{\mathbf{E}_u \times \mathbf{B}_u}{B_u^2}, \quad (15)$$

where subscript  $u$  represents the upstream boundary. Both electrons and ions are assumed to be frozen in the magnetic field in the upstream region, and the one-dimensional

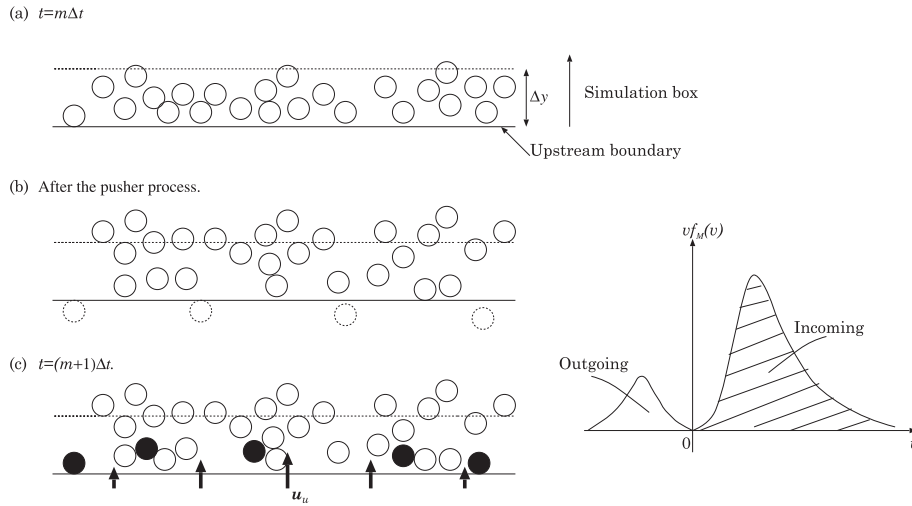


Fig. 3 Schematic illustration of the previous model of the upstream boundary for particles and the probability function of velocity. Distribution of particles: (a) at  $t = m\Delta t$ , (b) after the pusher process, and (c) at  $t = (m + 1)\Delta t$ . Open circles are particles, and closed circles are supplied particles. Dashed-line circles are removed particles.

inflow along the  $y$  direction is supplied to the system from an external region. Thus, the increase of mass flux is proportional to that of magnetic flux at the upstream boundary. Then, the change in the number density  $n_u$  at the input boundary can be expressed by the following relation:

$$n_u = n_u^0 \frac{B_u}{B_u^0}, \quad (16)$$

where superscript 0 indicates for the initial time.

In the previous model, the plasma is supplied from the upstream boundaries to the simulation domain at each time step with inflow velocity  $u_u$  and number density  $n_u$ . Figure 3 schematically shows the particle update procedure in the previous model. Particles (open circles) near the upstream boundary are supposed to exist as in Fig. 3 (a) at  $t = m\Delta t$ , where  $m$  is an integer. At the next step [ $t = (m + 1)\Delta t$ ], particle positions are updated according to the Newton-Lorentz equation (Eq. (1)), as shown in Fig. 3 (b). This procedure is called the pusher process [40]. Several particles near the upstream boundary move toward the center of the system by  $\mathbf{E} \times \mathbf{B}$  drift, and the number density decreases near the boundary. Then, particles (closed circles) are supplied through the upstream boundary, as shown in Fig. 3 (c), to conserve the number density  $n_u$ . If particles satisfy the shifted Maxwellian  $f_M(v)$  at the upstream boundary, particles with positive velocity come into the system, while those with negative velocity are lost from the system.

The probability of particles passing across the boundary surface in one time step is given as  $f_M(v)v\Delta t$  (see Fig. 3). Because the probability depends on time and space, that is, because the number density at the input boundary and the averaged inflow velocity change temporally and spatially (Eqs. (15) and (16)), we have to generate a particle ensemble that satisfies the probability function

at each time step and at each spatial position. However, to achieve high accuracy in numerical simulation by this method, many more particles than we can treat using a supercomputer are required. To avoid this difficulty, in the previous model, we expand the probability function into a function independent of the flow velocity  $u_u$  and some algebraic multiplier of  $u_u$  by assuming that  $u_u \ll v_T$ , where  $v_T$  is the thermal velocity. This process enables us to use a reservoir consisting of a huge number of particles for particle loading, independently of space and time.

If the total number of inflow particles to be loaded to each cell at each time step is small, the particles become a source of unphysical noise, which breaks the frozen-in condition at the upstream boundary, as shown in Sec. 5. For example, the average number of particles loaded per cell is about 2 in the 3-D case. Because it is difficult to increase the number of particles in large-scale simulations because computer resources are limited, and the loaded particles are also distributed in the  $z$  direction, the number becomes small. Even if the loaded particles are sampled randomly from the reservoir of the particle ensemble, such a small number of particles introduces noise. To load a sufficiently large number of inflow particles even with limited computer resources, we develop a new model that can reduce unphysical noise at the upstream boundary, as explained in the next paragraph. In the 2-D case, the number of inflow particles at the upstream boundary is large, because it is possible to set the number of particles per cell to be sufficient over the entire simulation box. Thus, this problem is not so severe in the 2-D case.

Next, we explain the improved new model of the upstream boundary, which we develop in this study. Figure 4 schematically illustrates the processes of the new model. First, let us define the  $Y$  boundary cells. They are located at  $y_b - \Delta y < |y| < y_b$ , where  $\Delta y$  is the grid size along the  $y$

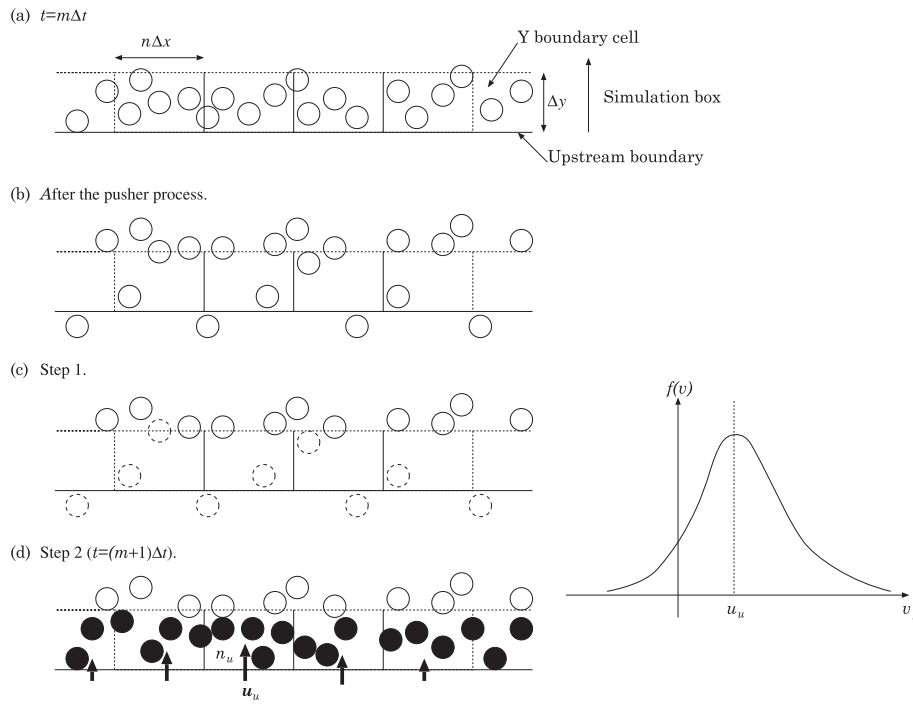


Fig. 4 Schematic illustration of the new model of the upstream boundary for particles and the velocity distribution function. Distribution of particles: (a) at  $t = m\Delta t$ , (b) after the pusher process, (c) step 1, and (d) step 2 of the new model at  $t = (m + 1)\Delta t$ .

direction. The cell is a parallelepiped whose length, width, and height are  $n\Delta x$ ,  $\Delta y$ , and  $2z_b$ , respectively. In this paper, an  $n$  value of 8 is adopted. Figure 4 (a) shows the position of particles near the upstream boundary at  $t = m\Delta t$ . The pusher process updates them, as shown in Fig. 4 (b). In step 1, the particles in the  $Y$  boundary cells are removed, as shown in Fig. 4 (c). The dotted circles in Fig. 4 (c) are the removed particles. In each  $Y$  boundary cell,  $u_u$  and  $n_u$  are calculated from Eqs. (15) and (16), respectively. Then, in step 2, particles with  $n_u$  and  $u_u$  (closed circles in Fig. 4 (d)) are newly loaded there based on the quiet-start technique [40]. The velocity distribution of the newly loaded particles rigorously obeys a shifted Maxwellian with constant temperature for every time step in each  $Y$  boundary cell. The spatial distribution of the loaded particles is uniform, and both electrons and ions are loaded at the same positions. Unequal numbers of electrons and ions are sometimes removed in step 1. In that case, the number of electrons or ions that are loaded is adjusted to satisfy charge neutrality in the entire system. If different numbers of electrons and ions are loaded, in some positions only electrons or ions are loaded, and an electrostatic field is locally generated at the upstream boundary. However, the difference in the numbers is small, and the generated electrostatic field is negligible because the frozen-in condition is preserved at the upstream boundary.

#### 4.2.2 Downstream boundary

At the open downstream boundary, particles can not only

leave but also enter the system across the boundary. Information about outgoing particles can be obtained directly by observing their motion at the boundary. The problems in the downstream boundary condition of particles are how many particles come into the system and how to assign the positions and velocities of these incoming particles. For the boundary condition of particles here, we assume that the physical state outside is the same as that in the boundary region. In other words, this assumption corresponds to a zero normal derivative condition, which is generally applied to the fluid moments in MHD [14, 15], Hall MHD [16, 17], and hybrid [35] simulations of reconnection. In these fluid simulations, the zero normal derivative condition is used for all variables (e.g.  $\partial/\partial x = 0$  and  $\partial/\partial y = 0$ ). However, a PIC simulation has infinite information, and many ambiguities are generated. Moreover, the velocity distribution function becomes non-Maxwellian in the downstream region as a result of the reconnection process. Accordingly, it is impossible for all quantities to satisfy the zero normal derivative condition and assume that the distribution of incoming particles is Maxwellian. At the least, we have to select the boundary condition that the zeroth, first, and second momenta should satisfy. In this section, we explain the previous and new models of boundary conditions under this assumption.

Figure 5 schematically illustrates the free boundary condition at a downstream boundary for particles that we adopted in the previous model. In this model, we make two assumptions. First, we assume that the net number flux of ions at the downstream boundary is the same as that of

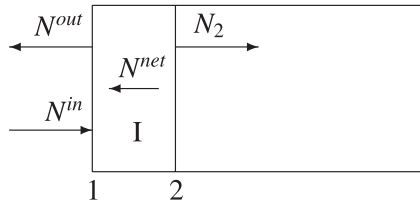


Fig. 5 Illustration of the previous downstream model, where  $N^{\text{net}}$ ,  $N^{\text{out}}$ ,  $N^{\text{in}}$ , and  $N_2$  are the net number of outgoing particles, the numbers of outgoing and incoming particles through the boundary, and the number of particles crossing inward through surface 2.

electrons, which is equal to the average net number flux in region I in Fig. 5. Second, we assume that the particle distribution function at position 1, that is, the downstream boundary, is the same as that at position 2. The details of the process in this model are as follows. We calculate the number of incoming particles across the open downstream boundary. The average particle velocity  $\bar{v}_x^1$  and number density  $n^1$  in region I (Fig. 5) are calculated. Next, we obtain the net number of outgoing particles passing across the boundary during one time step  $\Delta t$  in the system,

$$N^{\text{net}} = -n^1 \bar{v}_x^1 \Delta t S_d, \quad (17)$$

where  $S_d (= 2y_b 2z_b)$  is the area of region I. According to the charge neutrality condition, the net numbers of electrons and ions are the same. Thus, the numbers of incoming electrons and ions to the system are given as

$$N_e^{\text{in}} = N_e^{\text{out}} - N^{\text{net}}, \quad (18)$$

$$N_i^{\text{in}} = N_i^{\text{out}} - N^{\text{net}}. \quad (19)$$

Next, the positions and velocities of incoming particles have to be assigned. We have already assumed that the physical state outside is the same as that in region I. In other words, the particle distribution function outside is the same as that in region I. Thus, the positions and velocities of incoming particles can be defined using the information for particles crossing surface 2 from left to right (Fig. 5).

Figure 6 schematically shows the process of the new model for the open boundary condition of particles at the downstream boundary. First, let us define the  $X$  boundary cells. They are located at  $x_b - \Delta x < |x| < x_b$ , where  $\Delta x$  is the grid size along the  $x$  direction and corresponds to the first region in Fig. 6 (a). The cell is a parallelepiped whose length, width, and height are  $\Delta x$ ,  $2y_b$  and  $2z_b$ , respectively. At  $t = m\Delta t$ , the particles near the downstream boundary exist, as shown in Fig. 6 (a). According to the pusher process, the positions of particles are updated at  $t = (m + 1)\Delta t$  (Fig. 6 (b)). In step 1, the particles in the  $X$  boundary cell and outside the simulation box are removed; the removed particles are shown as dotted circles in Fig. 6 (c). To realize the assumption that the physical quantity outside is the same as that in the boundary region, we make the same particle distribution function in the  $X$  boundary cell as in the

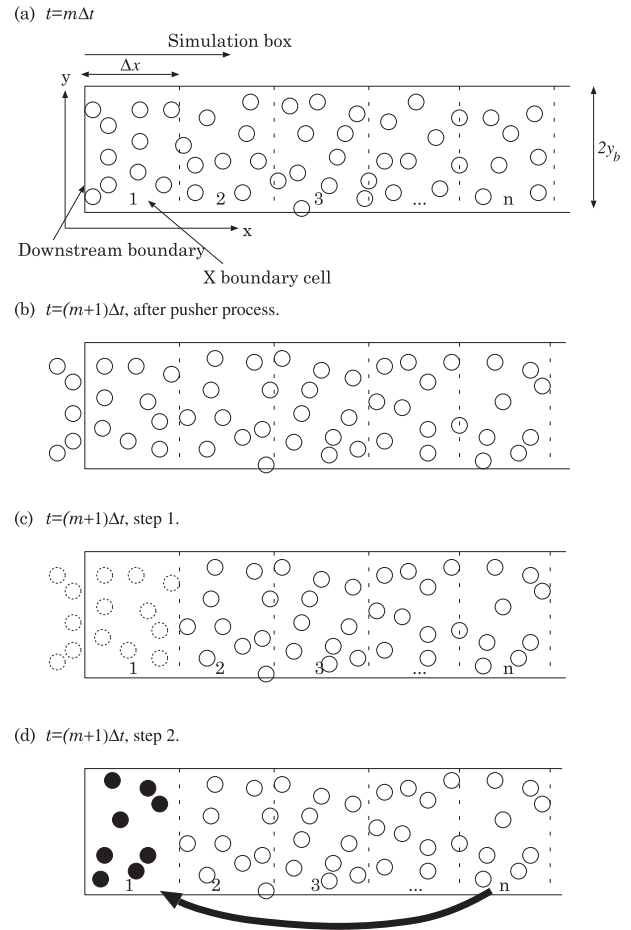


Fig. 6 Schematic illustration of the new model of the downstream boundary for particles. Distribution of particles: (a) at  $t = m\Delta t$ , (b) after the pusher process, (c) step 1, and (d) step 2 of the new model at  $t = (m + 1)\Delta t$ .

$n$ -th region, which is the  $(n-1)$ -th neighbor of the  $X$  boundary cell. The positions and velocities of particles (closed circles in Fig. 6 (d)) in the  $X$  boundary cell are defined using the information for particles in the  $n$ -th region (for example,  $n = 5$ ). Thus, in this step, all the particles in the  $X$  boundary cell are replaced by those in the  $n$ -th region. Unequal numbers of electrons and ions are sometimes removed in step 1. In that case, the number of electrons or ions are loaded in the  $X$  boundary cell is adjusted to satisfy charge neutrality in the entire system. If particles move from the  $(n-1)$ -th region to the  $n$ -th region, the velocities and positions of these particles in the  $n$ -th region can be used to specify the information on newly incoming particles from the downstream boundary in the  $X$  boundary cell. In this model, the variation of particle quantities along the  $x$  direction nearly vanishes at the boundary. Accordingly, the zero normal condition is realized there.

We compare the results of the new and previous models in Sec. 5 and show the advantages of the new model in Sec. 6.

## 5. Comparison of New and Old Models

In this section, we compare the time evolution of magnetic reconnection in the new and previous boundary models (C1 and C2 cases, respectively, in Table 1) in 3-D simulation. Simulation parameters are as follows: The mass ratio  $m_i/m_e$  is 100, and the driving field  $E_{z0}$  is  $-0.04B_0$ , where  $B_0$  is a constant. The scale length of current layer  $L$  is  $0.787\rho_i$  at the initial time, where  $\rho_i$  is the ion Larmor radius defined using magnetic field  $B_0$ . The thermal velocities of electrons and ions are  $0.268c$  and  $0.0268c$ , respectively. The ratio of the plasma frequency to the gyrofrequency for electrons  $\omega_{pe}/\omega_{ce}$  is 2, and the time step  $\omega_{ce}\Delta t$  is 0.067.

### 5.1 Upstream

Figure 7 shows the time evolution of (a) the reconnection electric field  $E_z$  and (b) the current density  $J_z$  at the reconnection point. The solid and dashed lines indicate the new (C1) and previous (C2) models, respectively. Let us compare the physical quantities of C1 and C2 until the reconnection electric field  $E_z$  starts increasing ( $0 < \omega_{ce}t < 400$ ). During this time, the driving electric field imposed at the upstream boundary penetrates into the current sheet because of particle kinetic effects. When the electric field reaches the neutral sheet, collisionless reconnection is triggered [28]. In  $\omega_{ce}t < 400$ , the time evolution of the physical quantities of the new model (C1) is almost the same as that of the previous model (C2). After  $E_z$  reaches the minimum value, the difference in each physical quantity between C1 and C2 increases. In the early time before  $E_z$  reaches the minimum value, the boundary condition does not influence the physics at the reconnection point because the reconnection point is far from the boundary. For this reason, the time evolution of the physical quantities is not so different between the new and previous models early in the simulation.

Figures 8 and 9 show the contour plots of the frozen-in condition  $\mathbf{E} + \mathbf{v} \times \mathbf{B}$  for electrons and ions, respectively, under the previous and new conditions. Figure 10 shows the profiles of  $\mathbf{E} + \mathbf{v} \times \mathbf{B}$  along the  $y$  direction passing the X point. When the frozen-in condition is satisfied, the quantity  $\mathbf{E} + \mathbf{v} \times \mathbf{B}$  becomes zero. The figures show that

Table 1 Simulation parameters.  $2x_b, 2y_b, 2z_b$  are the size of simulation box.  $\rho_i$  is the ion Larmor radius.  $N_x, N_y, N_z$  are the numbers of grids along the  $x, y,$  and  $z$  axes, respectively.  $N_{p0}$  is the number of the particles that compose the Harris equilibrium at the initial time.

	$2x_b, 2y_b, 2z_b$ ( $/\rho_i$ )	$N_x, N_y, N_z$	$N_{p0}$	Boundary
C1	12.7, 6.35, 9.60	130,129,130	32million	new
C2	12.7, 6.35, 9.60	130,129,130	32million	previous
C3 (short)	25.4, 6.35, 2.40	258,129,36	16million	new
C4 (long)	102, 6.35, 2.40	1026,129,36	64million	new

$\mathbf{E} + \mathbf{v} \times \mathbf{B}$  is almost zero near the upstream boundary for both electrons and ions in the new model. On the other hand,  $\mathbf{E} + \mathbf{v} \times \mathbf{B}$  remains finite in the previous model.

From Figs. 8, 9, and 10, we can explain why  $E_z$  and  $J_z$  show different tendencies in the previous and new models after  $E_z$  reaches the minimum value. In the previous model, when mild unphysical noise is generated near the upstream boundary, as shown in the figures, it is carried toward the central region with incoming plasma flow and disrupts the physics of reconnection after it reaches the reconnection point. In the new model, on the other hand, the frozen-in condition is satisfied with high accuracy, and unphysical noise is not generated in the region of the upstream boundary. Therefore the difference in physical quantities increases after reconnection occurs.

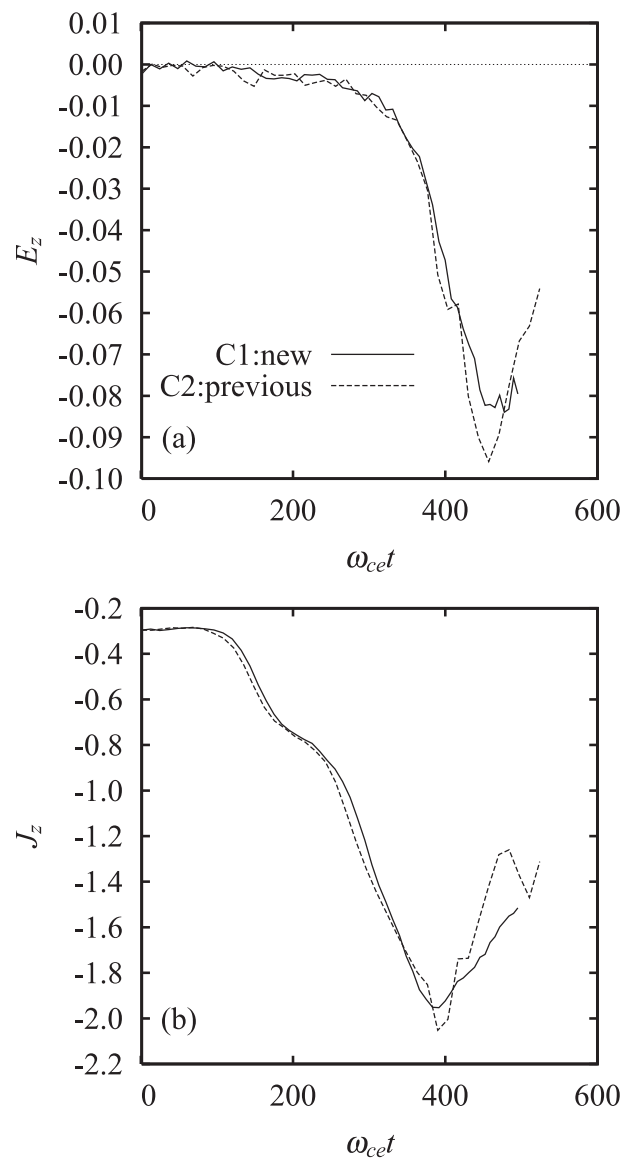


Fig. 7 Time evolution of (a) the reconnection electric field  $E_z$ , and (b) the current density  $J_z$ . Solid and dashed lines show the cases of C1 and C2, respectively.

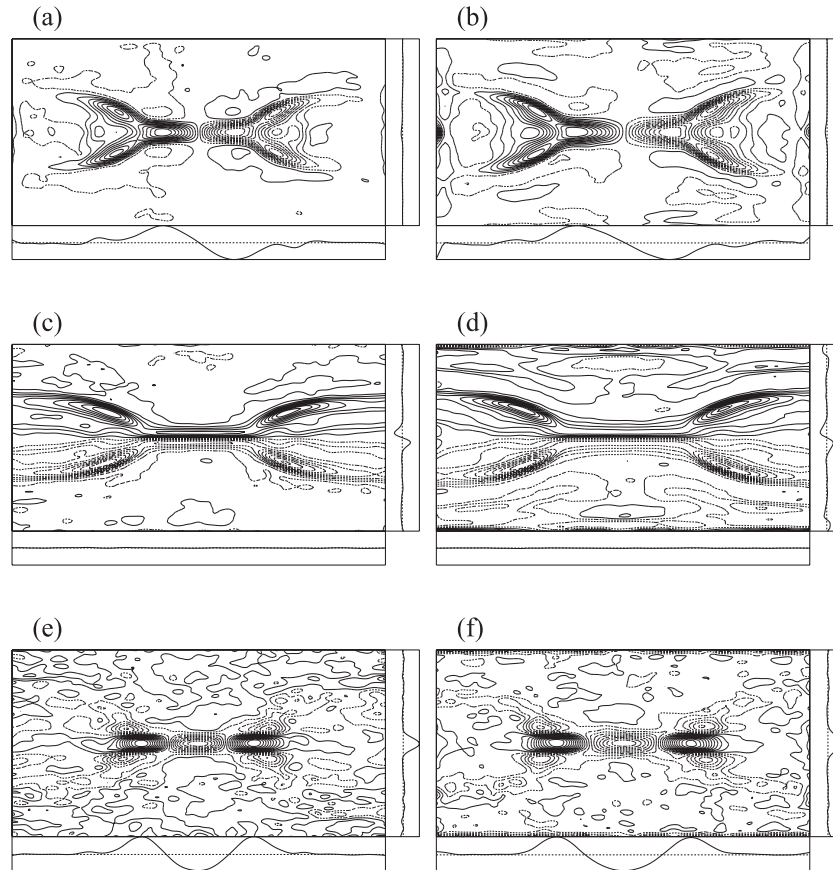


Fig. 8 Contour plots of  $\mathbf{E} + \mathbf{v} \times \mathbf{B}$  of electrons in the  $xy$  plane at  $\omega_{ce}t = 492$ . Left and right figures show the cases of the new and previous models, respectively. Top, middle, and bottom panels show the  $x$ ,  $y$ , and  $z$  components of  $\mathbf{E} + \mathbf{v} \times \mathbf{B}$ , respectively. Horizontal axis is  $x$ , and vertical axis is  $y$ . Right and bottom side panels show the profile along the  $y$  direction at  $x = 0$  and along the  $x$  direction at  $y = 0$ , respectively.

The reasons that the accuracy near the upstream boundary increases in the new model compared with the previous one are as follows. In the previous model, the number of particles supplied from the upstream boundary in one time step is small in 3-D simulation, for example, 1 or 2 per cell at most. Accordingly, the distribution formed by the supplied particles becomes disordered. In the previous model, moreover, the velocity distribution function of the supplied particles is obtained under the assumption  $u_{\parallel} \ll v_T$ . However, the flow velocity of ions induced by the  $\mathbf{E} \times \mathbf{B}$  drift is marginally less than the ion thermal velocity, so the assumption is not appropriate. For these reasons, it is considered that unphysical noise is created and breaks the frozen-in condition at the upstream boundary in the previous model. Under the new boundary, on the other hand, all the particles in all boundary cells at the upstream boundary are exchanged at every time step for refreshed particles, whose distribution is determined by the quiet-start technique [40] so as to satisfy the shifted Maxwellian rigorously. In this way, particles with an orderly distribution are loaded, and the particles at the upstream boundary are refreshed at all times. As a result, the frozen-in condition is always satisfied at the upstream boundary with high

accuracy even in 3-D simulation.

## 5.2 Downstream

In this subsection, we compare the results obtained from the new and previous downstream models. Figures 8 and 9 show that the contour plots of the  $y$  and  $z$  components of  $\mathbf{E} + \mathbf{v} \times \mathbf{B}$  are smooth, while the  $x$  component is disordered at the downstream boundary for both electrons and ions in the previous model. The positions and velocities of incoming particles through the downstream boundary are obtained from the information on particles crossing surface 2 from left to right (Fig. 5) in the previous model. The number of supplied incoming particles per cell is small in the case of 3-D simulation, and thus, numerical noise is generated. In the new model, on the other hand, the information for all particles in the boundary region ( $X$  boundary cell) is replaced by that in the  $n$ -th neighbor cell at each time step. As a result, incoming particles are not directly dealt with as the particles supplied from the downstream boundary as in the previous model. Accordingly, numerical noise is not generated in the downstream boundary in the new model.

In this paper, we compare the 3-D simulation results

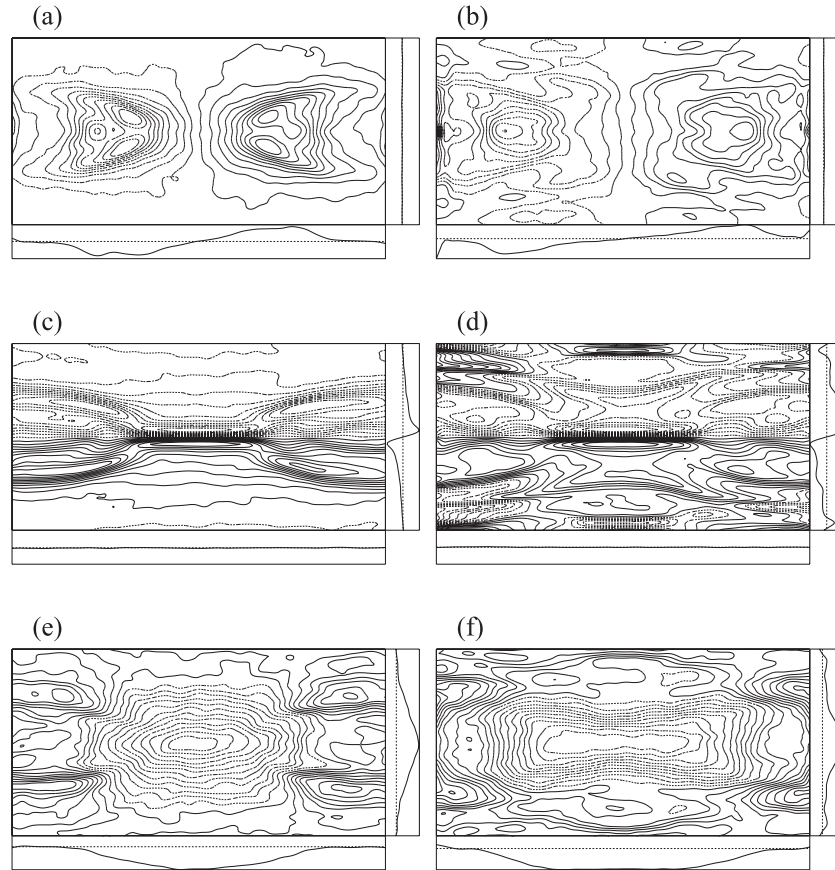


Fig. 9 The same figure as Fig. 8 but of ions.

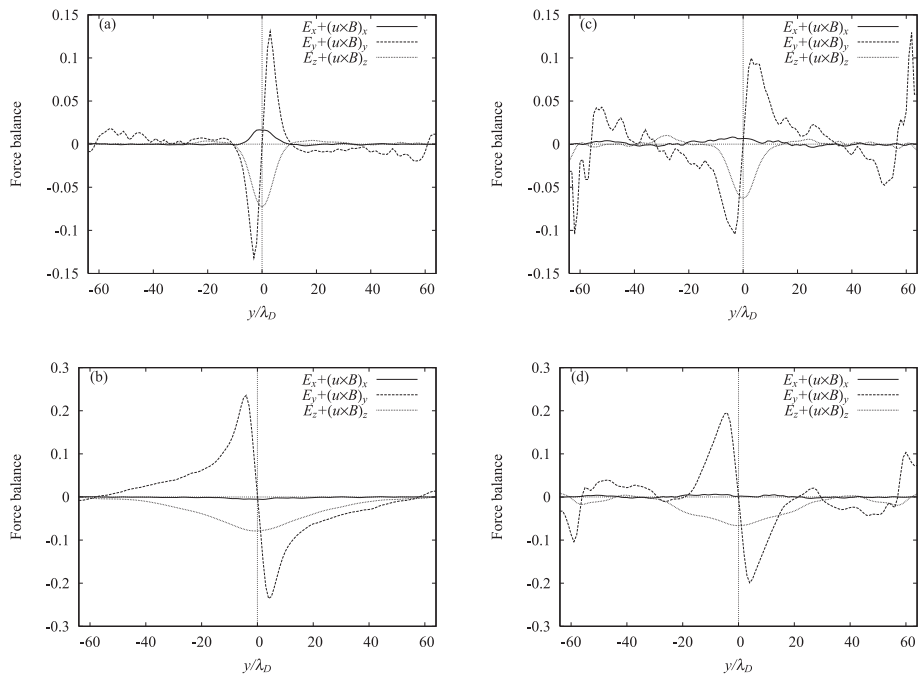


Fig. 10 Profiles of  $\mathbf{E} + \mathbf{u} \times \mathbf{B}$  along the  $y$  direction passing X point for (a) electrons and (b) ions in case C1, and (c) electrons and (d) ions in case C2. Solid, broken, and dotted lines show  $x$ ,  $y$ , and  $z$  components, respectively.

obtained from the new and previous models under the same conditions, e.g., the same number of particles per cell. Even in the previous model, there is no difficulty in satisfying the frozen-in condition in the upstream region or the smoothness of the physical quantities in the downstream region, when the number of particles per cell is sufficient. However, it is difficult to increase the number in large-scale simulations because computer resources are limited. Accordingly, it is important to develop models, such as this new model, which can reduce unphysical noise at the boundary, even though the number is small. In the case of 2-D simulation using the previous model, the numbers of inflow particles supplied from the upstream boundary and incoming particles through the downstream boundary are large, because the number of particles per cell is adequate. Thus there is no problem in 2-D simulation with the previous model.

## 6. Validity of Downstream Model

Next, we compare the simulation results for short and long simulation boxes (C3 and C4 in Table 1) to check the validity of the new downstream model. A very long current sheet ( $102\rho_i$ ) along the outflow direction ( $x$ ) is set up in the long-simulation box, while a short current sheet ( $25.4\rho_i$ ) is used in the short-simulation box. Driven reconnection takes place at the center of the simulation box for both the long and short simulation boxes. In the downstream model, the positions and velocities of particles in the  $X$  boundary cell are defined using the information for particles in the second region in this test simulation. If the downstream boundary model is effective, the results of the short-simulation box should mimic those in the corresponding part of the long-simulation box.

We first examine the time evolution of the current density  $J_z$  and electric field  $E_z$  at the  $X$  point. Figure 11 shows that both  $J_z$  and  $E_z$  in the short-simulation box are almost the same as in the long-simulation box. This means that the time evolution of reconnection dynamics at the  $X$  point of the two cases is in good agreement. Figure 12 shows snapshots of the magnetic field at  $t\omega_{ce} = 680$ . The magnetic field structures in the cases of the short and long simulation boxes are consistent. Next, let us compare several physical quantities. Figures 13 and 14 show the magnetic flux  $\phi$ , flow pattern  $\mathbf{u}$ , and temperature  $T$  at  $t\omega_{ce} = 805$  in the cases of long and short simulation boxes. Here the magnetic flux  $\phi$  is defined such that  $\mathbf{B}_\perp = \hat{\mathbf{z}} \times \nabla\phi$ , and is calculated from the averaged values  $\bar{B}_x$  and  $\bar{B}_y$  along the  $z$  direction, where  $\perp$  denotes the  $x$  and  $y$  components. Every variable shows the same pattern. Finally, we compare them quantitatively. Figure 15 displays the profiles of the frozen-in condition  $\mathbf{E} + \mathbf{u} \times \mathbf{B}$  along the  $x$  direction passing the  $X$  point. The positions of peaks and the tendency of every quantity in the case of the short simulation box are in good agreement with those of the long simulation box.

All of these data show that the new downstream

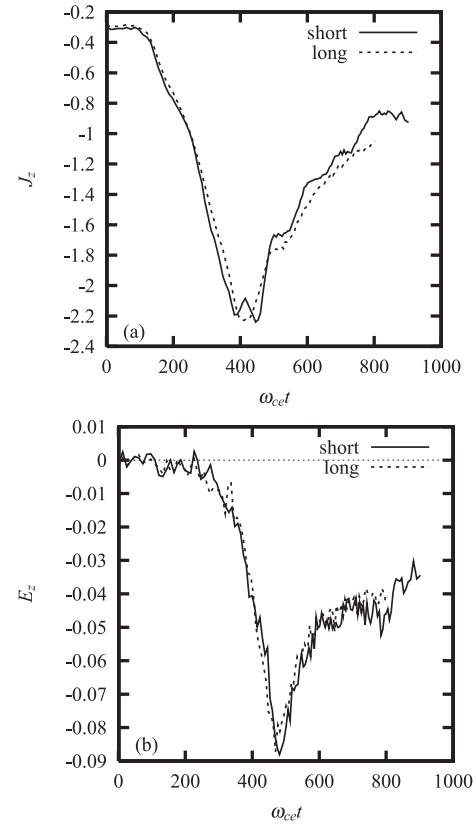


Fig. 11 Time evolutions of (a) current density  $J_z$  and (b) electric field  $E_z$  at the  $X$  point, where solid and broken lines show results for cases C3 and C4, respectively.

boundary model works very well at least until  $t\omega_{ce} = 800$ . To learn whether reconnection is steady or non-steady, we need to perform the simulation a factor of 10-30 times longer. Information on particles in the second neighbor cell is used to specify the newly loaded particles in the  $X$  boundary cell in this test simulation. Since the second neighbor cell is a near neighbor to the  $X$  boundary cell, and the newly incoming particles are just copies of particles that are already in the near cell, it is considered that a small perturbation near the boundary can feed back upon itself. This will introduce unphysical correlations at longer time-scales. To avoid this feedback, it will be necessary to set the sampling region far from the  $X$  boundary. In our next paper, we will discuss the dependence on the position of the sampling region of information on particles in the  $X$  boundary cell, and the validity of this downstream model over more physically interesting time scales.

## 7. Summary and Conclusions

A new open boundary model for 3-D electromagnetic particle simulation is developed to investigate magnetic reconnection in an open system. Because a very large CPU memory size is needed for the simulation, this simulation code is also programmed to work effectively on a distributed memory and processor computer system with a

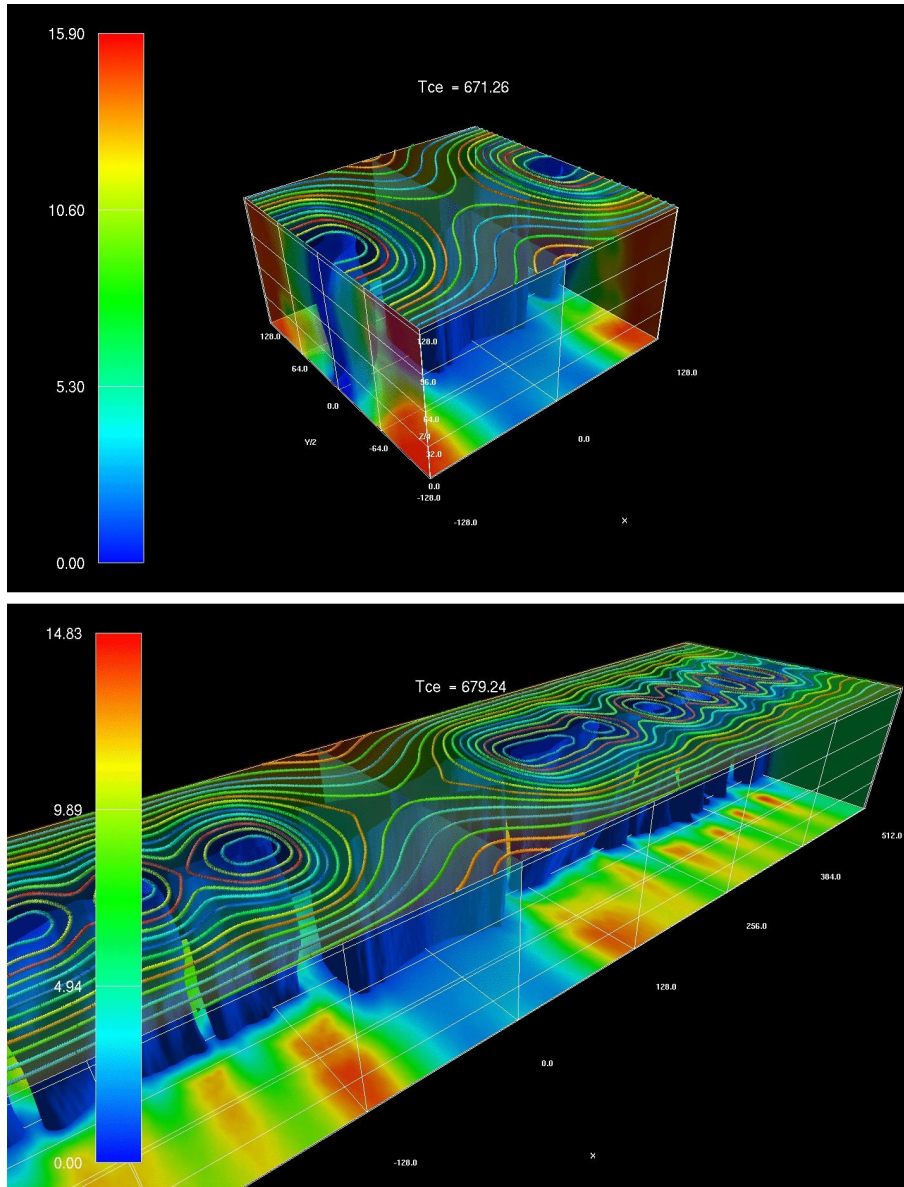


Fig. 12 Snapshot of magnetic structure at  $t\omega_{ce} = 680$ . Top and bottom figures show the results for the short and long simulation boxes, respectively. Color isolines on top plane show the magnetic flux  $\phi$ , and isosurfaces and color contours on the bottom plane show  $B_x^2 + B_y^2$ .

distributed parallel algorithm. PASMO is parallelized with High Performance Fortran [39]. For data layout, all field data are duplicated in each parallel process, but particle data are distributed among them [44]. We invent an algorithm for the open boundary of particles, in which an operation for outgoing and incoming particles is performed in each processor, and the only reduction operation for the number of particles is executed during data transfer. This adequate treatment makes the amount and frequency of data transfer small and the load balance among processes relevant.

An open boundary condition is essential for long-term collisionless reconnection behaviors such as steady reconnection and intermittent reconnection [26]. A periodic

boundary condition has been used thus far in the outflow direction. However, it generates an artificial flow from the downstream boundary and distorts the physics of reconnection for a long time. The problem of the open boundary model is how particles enter and leave the system. Several open boundary models have already been proposed as a downstream boundary model [25–27, 34–38]. Let us compare our model with them. Ding *et al* [34] used 2-D PIC simulation to investigate driven reconnection. Outgoing plasma flow generated during magnetic reconnection went freely from the simulation domain through the downstream boundary. Pritchett *et al* [36, 45] employed a 2-D PIC model for the case of driven reconnection. Their open boundary for the particles meant that particles cross-

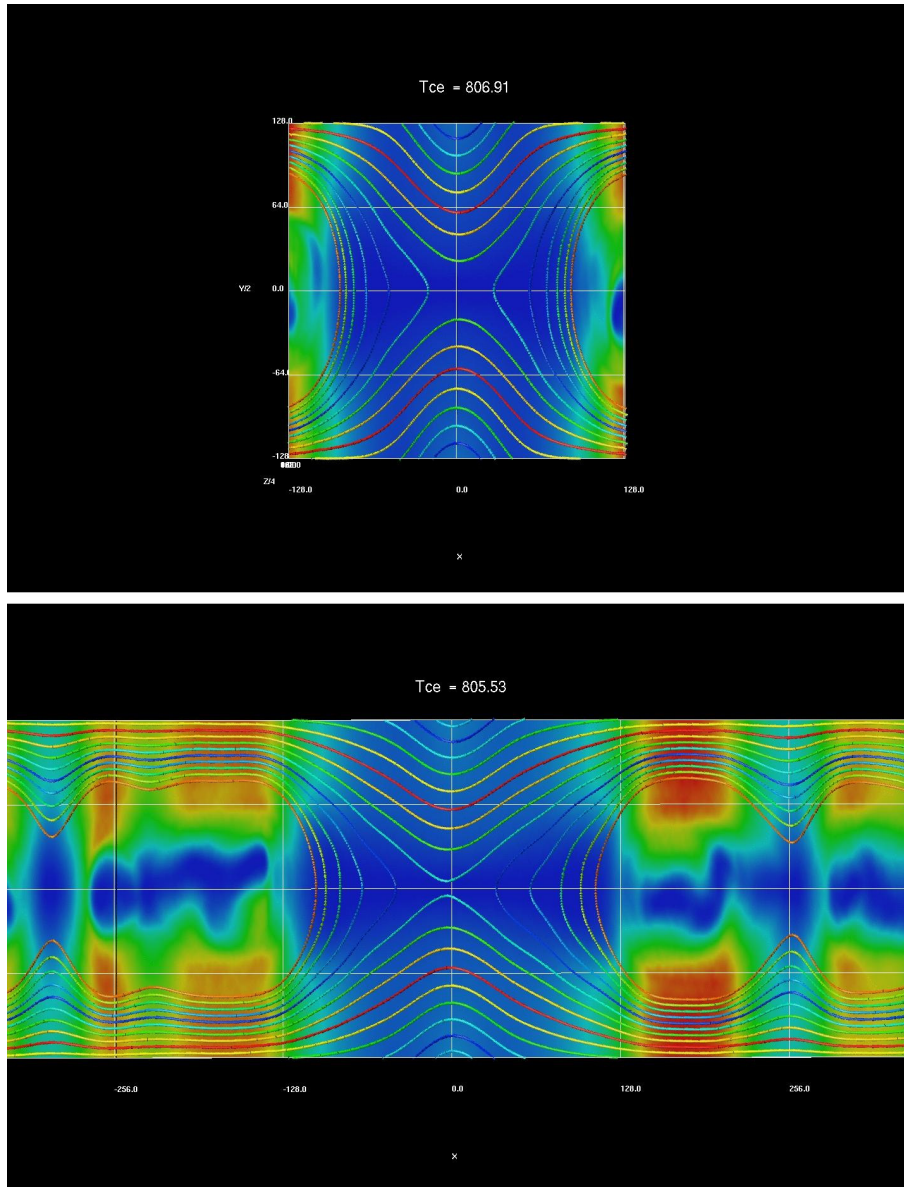


Fig. 13 Magnetic field structure for the short (top) and long (bottom) simulation boxes. In the case of long simulation box, the region corresponding to the short simulation box is enlarged. Color isolines show the magnetic flux  $\phi$  and color contours show  $B_x^2 + B_y^2$ .

ing the downstream boundary were removed from the system, and that new particles were injected into the system at a constant rate based on a thermal Maxwellian distribution. Krauss-Varban *et al* [35] used inflow-outflow boundary conditions, where plasma is free to flow in or out, in 2-D and 3-D electromagnetic hybrid codes. A zero gradient was maintained in the first two momenta of the ion distribution in an approximate manner. Daughton *et al* [37] assumed that the distribution function in the region near the boundary was approximately given by a quadratic form. Using this approximated distribution function, they obtained the incoming flux of particles with normal velocity, the total number of particles injected from the boundary, and transverse velocity components. They studied spontaneous reconnection under this condition in 2-D simula-

tion. Klimas *et al* [38] also assumed that particle distributions have zero normal derivatives at the boundary. In their method, the position and velocity of each particle is stored in the column at the boundary. If a particle moves from this column to the next inside column, an identical particle outside of the boundary is assumed to have moved into the column at the boundary. This method is similar to our previous model in that they used the information of particles crossing the surface as the positions and velocities of incoming particles [25–27]. They also studied spontaneous reconnection in a 2-D simulation by this method.

In all the models including Pei's model [25–27], the method of dealing with outgoing particles is the same; that is, when a particle crosses a boundary in the outward direction, it is permanently lost. It is important to estimate

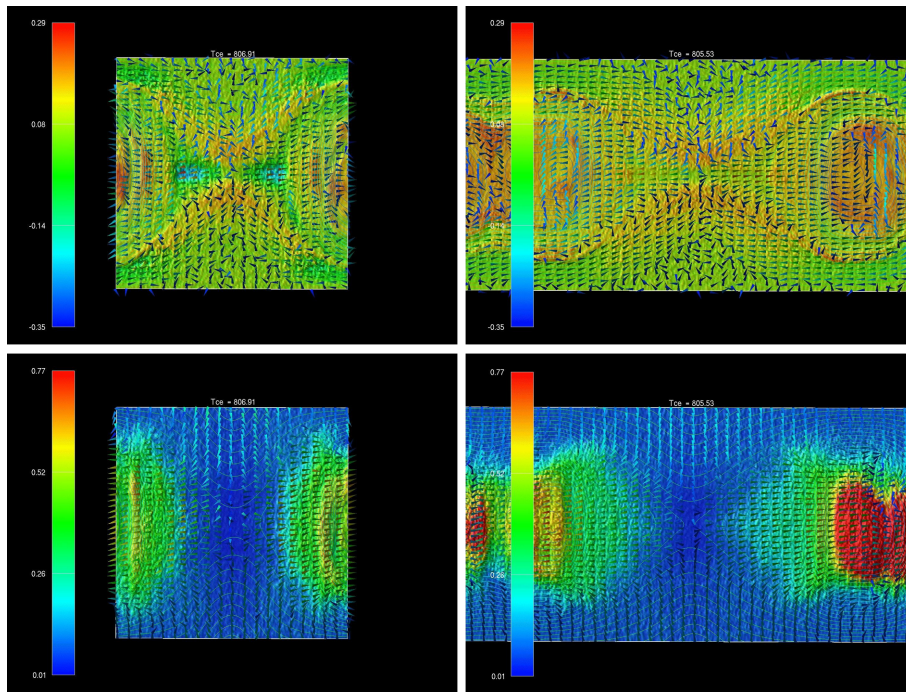


Fig. 14 Flow pattern and temperature profile in the  $(x, y)$  plane. Left and right figures show the cases of short and long simulation boxes, respectively. Top and bottom show the cases of electrons and ions, respectively. In the case of the long simulation box, the region corresponding to the short simulation box is enlarged.

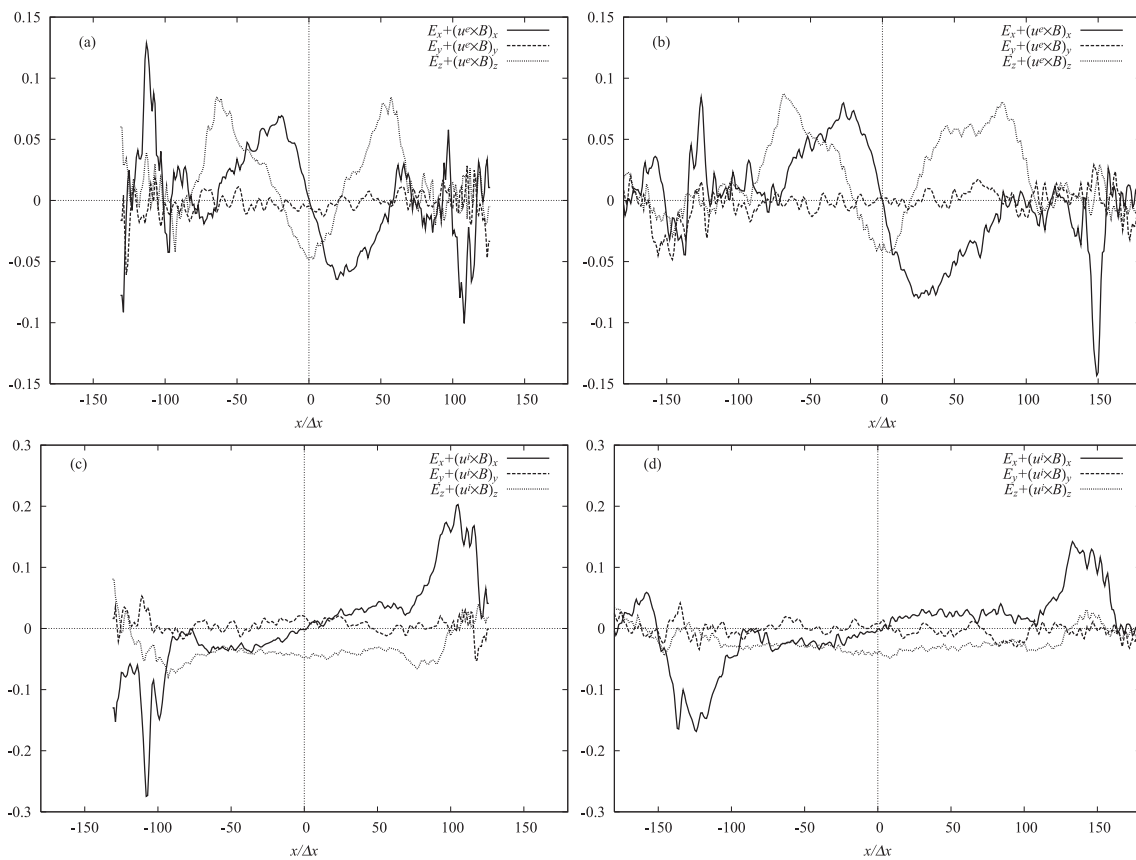


Fig. 15 Profile of  $\mathbf{E} + \mathbf{u} \times \mathbf{B}$  along the  $x$  direction for (a) electrons and (b) ions for C3, and (c) electrons and (d) ions for C4. Solid, dashed, and dotted lines show  $x$ ,  $y$ , and  $z$  components of  $\mathbf{E} + \mathbf{u} \times \mathbf{B}$ , respectively. In the case of the long simulation box, the region corresponding to the short simulation box is enlarged.

the number and distribution of incoming particles, instead of enforcing a boundary condition on the momenta as in MHD, Hall MHD, and hybrid simulations [14–17, 35]. In the model of Ding *et al* [34], particles incoming through the downstream boundary were not considered. Accordingly, an inward flux was not considered and a zero normal derivative condition was not preserved there. The model of Pritchett *et al* [36, 45] assumed that incoming particles came through the boundary at a constant rate based on a simple Maxwellian distribution. This model cannot estimate a net flux correctly at the downstream boundary. Krauss-Varban *et al* [35] and Daughton *et al* [37] approximated the distribution function near the boundary. When these approximations are exact, the inward flux is calculated correctly. On the other hand, although our model does not assume a specific form of distribution function at the downstream boundary, both the inflow and outflow fluxes are estimated and the zero normal derivative condition is preserved, because the information for particles in the  $X$  boundary cell is the same as that for those in its  $n$ -th neighbor cell. Our model is much simpler than other models, but it is effective, as shown in Sec. 6. It will be interesting to compare their results in future to investigate the influence of boundary conditions on the physics of reconnection.

## Acknowledgments

This work is supported by Grant-in-Aids for Scientific Research (No. 18340188) and for Young Scientists (B) (No. 19740346) from the Japan Society for the Promotion of Science (JSPS), and the Research Cooperation Program on “Hierarchy and Holism in Natural Sciences 2” at the National Institutes of Natural Sciences. It is also performed with the support and under the auspices of the National Institute for Fusion Science (NIFS) Collaborative Research Program (NIFS08KTAN004).

- [1] V.A. Sergeev, V. Angelopoulos, D.G. Mitchell and C.T. Russell, *J. Geophys. Res.* **100**, 19121 (1995).
- [2] A.T.Y. Lui, *IEEE Trans. Plasma Sci.* **28**, 1854 (2000).
- [3] Y. Ono, M. Inomoto, T. Okazaki and Y. Ueda, *Phys. Plasmas* **4**, 1953 (1997).
- [4] M. Yamada, *Phys. Plasmas* **14**, 058102 (2007).
- [5] D. Biskamp, *Magnetic Reconnection in Plasmas* (Cambridge University Press, Cambridge, 2000).
- [6] E. Priest and T. Forbes, *Magnetic Reconnection MHD Theory and Application* (Cambridge University Press, Cambridge, 2000).
- [7] H.P. Furth, J. Killeen and M.N. Rosenbluth, *Phys. Fluids* **6**, 459 (1963).
- [8] B. Coppi, G. Laval and R. Pellat, *Phys. Rev. Lett.* **16**, 1207 (1966).
- [9] J.F. Drake and Y.C. Lee, *Phys. Fluids* **20**, 1341 (1977).
- [10] I. Katanuma and T. Kamimura, *Phys. Fluids* **23**, 2500 (1980).
- [11] W. Zwingmann, J. Wallace, K. Schindler and J. Birn, *J. Geophys. Res.* **95**, 20877 (1990).
- [12] P.L. Pritchett, F.V. Coroniti, R. Pellat and H. Karimabadi, *J. Geophys. Res.* **96**, 11523 (1991).
- [13] X. Wang and A. Bhattacharjee, *J. Geophys. Res.* **98**, 19419 (1993).
- [14] M. Scholer, *J. Geophys. Res.* **94**, 8805 (1989).
- [15] T.G. Forbes and E.R. Priest, *Rev. Geophys.* **25**, 1583 (1987).
- [16] J.D. Huba and L.I. Rudakov, *Phys. Rev. Lett.* **93**, 175003 (2004), hall MHD simulation in open system.
- [17] J.D. Huba, *Phys. Plasmas* **12**, 012322 (2005).
- [18] R. Horiuchi, K. Nishimura, T.H. Watanabe and T. Sato, *Nucl. Fusion* **39**, 2083 (1999).
- [19] M. Hesse, K. Schindler, J. Birn and M. Kuznetsova, *Phys. Plasmas* **6**, 1781 (1999).
- [20] M. Hesse, J. Birn and M. Kuznetsova, *J. Geophys. Res.* **106**, 3721 (2001).
- [21] P. Ricci, J.U. Brackbill, W. Daughton and G. Lapenta, *Phys. Plasmas* **11**, 4102 (2004).
- [22] M.A. Shay, J.F. Drake and M. Swisdak, *Phys. Rev. Lett.* **99**, 155002 (2007).
- [23] K. Fujimoto and S. Machida, *J. Comp. Phys.* **214**, 550 (2006).
- [24] K. Fujimoto, *Phys. Plasmas* **13**, 072904 (2006).
- [25] R. Horiuchi, W. Pei and T. Sato, *Earth, Planets and Space* **53**, 439 (2001).
- [26] W. Pei, R. Horiuchi and T. Sato, *Phys. Plasmas* **8**, 3251 (2001).
- [27] W. Pei, R. Horiuchi and T. Sato, *Phys. Rev. Lett.* **87**, 235003 (2001).
- [28] R. Horiuchi, H. Ohtani and A. Ishizawa, *Comp. Phys. Comm.* **164**, 17 (2004).
- [29] A. Ishizawa, R. Horiuchi and H. Ohtani, *Phys. Plasmas* **11**, 3579 (2004).
- [30] A. Ishizawa and R. Horiuchi, *Phys. Rev. Lett.* **95**, 045003 (2005).
- [31] R. Horiuchi, H. Ohtani and A. Ishizawa, *J. Plasma Phys.* **72**, 953 (2006).
- [32] H. Ohtani, R. Horiuchi and A. Ishizawa, *J. Plasma Phys.* **72**, 929 (2006).
- [33] A. Ishizawa and R. Horiuchi, *J. Plasma Phys.* **72**, 787 (2006).
- [34] D. Ding, L. Lee and D. Swift, *J. Geophys. Res.* **97**, 8453 (1992).
- [35] D. Krauss-Varban and N. Omid, *Geophys. Res. Lett.* **22**, 3271 (1995).
- [36] P.L. Pritchett, *J. Geophys. Res.* **106**, 3783 (2001).
- [37] W. Daughton, J. Scudder and H. Karimabadi, *Phys. Plasmas* **13**, 072101 (2006).
- [38] A. Klimas, M. Hesse and S. Zenitani, *Phys. Plasmas* **15**, 082102 (2008).
- [39] H. Ohtani *et al.*, *Lecture Notes in Computer Science* **4759**, 329 (2008).
- [40] C.K. Birdsall and A.B. Langdon, *Plasma Physics Via Computer Simulation* (McGraw-Hill, New York, 1985).
- [41] E.G. Harris, *Nuovo Cimento* **23**, 115 (1962).
- [42] I. Shinohara, H. Suzuki, M. Fujimoto and M. Hoshino, *Phys. Rev. Lett.* **87**, 095001 (2001).
- [43] W. Daughton, *Phys. Plasmas* **6**, 1329 (1999).
- [44] B.D. Martino, S. Briguglio, G. Vladb and P. Sguazzeroc, *Parallel Computing* **27**, 295 (2001).
- [45] P.L. Pritchett, *J. Geophys. Res.* **110**, A10213 (2005).